# Two-Segment Three-Phase PMSM Drive With Carrier Phase-Shift PWM for Torque Ripple and Vibration Reduction

Xun Han, *Student Member, IEEE*, Dong Jiang, *Senior Member, IEEE*, Tianjie Zou, *Student Member, IEEE*, Ronghai Qu, *Fellow, IEEE*, and Kai Yang

***Abstract*—This paper presents a two-segment motor system powered by two inverters with phase-shift pulsewidth modulation (PWM) to fulfill the purpose of low-torque ripple and vibration noise. Different from conventional multi-inverter structure, the inverters for this type of machine are electrically isolated between each other. First, the concept of multisegment machine is presented and the basic operation principle is analyzed with finite-element analysis (FEA) method. Then vibration caused by the switching device in machine is investigated and the control model of a two-segment motor is developed. Further, the principle of carrier phase-shift PWM is illustrated with the vibration analysis. Carrier phase shift can generate interleaved torque and force on the rotor for the two groups of windings in the machine and cancel each other for certain harmonics. Then simulation of control strategy for this type of machine has been done in MATLAB. Finally, based on the concept and principles mentioned before, a two-segment motor with its drive system is fabricated. Both the test of torque ripple and the vibration of the motor have been significantly improved. Compared with a normal three-phase motor driven by a paralleled inverter with interleaving, the proposed approach is with comparable vibration reduction but without using extra coupled inductors.**

***Index Terms*—Carrier phase-shift pulsewidth modulation (PWM), torque ripple reduction, two-segment motor.**

## I. Introduction

DUE to the superior performance of rare earth permanent-magnet (PM) material, PM synchronous machines (PMSMs) have been widely used in recent years. Apart from power density and efficiency, torque smoothness is another important criterion in many PMSM applications, including traction, machine tool, and power steering. Torque smoothness issue has been extensively studied in literature [1]. Generally, the torque pulsation of a PMSM consists of the inherent cog-

Manuscript received October 15, 2017; revised January 16, 2018; accepted March 29, 2018. Date of publication April 8, 2018; date of current version November 19, 2018. This work was supported by Delta Electronics Foundation under Project DREK201703. Recommended for publication by Associate Editor D. G. Xu. *(Corresponding author: Dong Jiang.)*

The authors are with the State Key Laboratory of Advanced Electromagnetic Engineering and Technology, School of Electrical and Electronic Engineering, Huazhong University of Science and Technology, Wuhan 430074, China (e-mail:

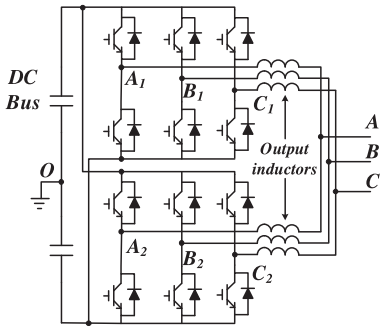


Fig. 1. Paralleled inverters.

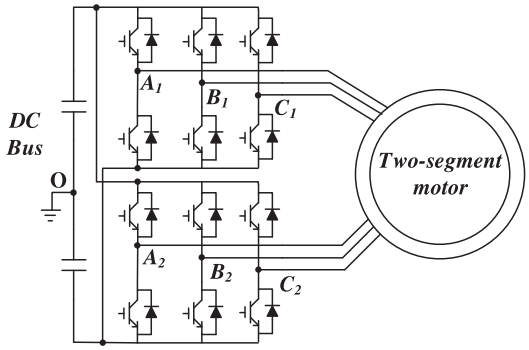


Fig. 2. Schematic of two-segment PMSM drive.

the two segments of the stator windings, too. Different from the paralleled structure of Fig. 1 for a regular three-phase motor, the paralleling of two converters are directly through the machine itself and no extra output inductor is needed. With the method of interleaving, the phase of current ripple in each three-phase winding can be shifted, thus making total torque ripple reduced.

The paper is structured as follows. First, the structure and principle of the two-segment PMSM system is introduced in part II. Then, vibration and torque ripple mitigation with PWM carrier shift method is discussed in Section III. It is supported by simulation in Section IV. Then, with a prototype motor drive, experimental results are presented in Section V. Final conclusions are summarized in Section VI.

## II. Operation Principle of the Two-Segment PMSM System

The method two-segment motor is induced here with the comparison to the method of paralleled converters.

### A. Conventional Paralleled VSIs Drive System

In the practical power transmission applications, modular VSIs have been widely used to achieve higher power by building modules. Normally, inverter paralleling is the primary method. The simple system of two paralleled inverters has been shown in Fig. 1, two paralleled VSIs are connected to a common ac bus through output inductors, and the three-phase ac machine is powered by two inverters simultaneously. The naming for variables and devices are marked in the diagram. As mentioned before, this structure can increase output power compared to conventional single-inverter structure and with carrier phase-shift (or "interleaving") method, current harmonics in the total current output side can be reduced a lot as well.

Through the double-integral Fourier analysis, taking phase A for example, the output side single-phase voltage between the ac terminal (e.g., point A1) and the dc-link midpoint ($O$) $v_{A1O}$ can be expressed by a series of harmonics [15]. The frequencies of harmonic components can be summarized as $m\omega_c + n\omega_0$, where $\omega_c$ is the angular frequency of the carrier wave, $\omega_0$ is the angular fundamental frequency of the voltage, and $m$ and $n$ are the carrier and baseband integer indices, respectively. Generally, the harmonic component of voltages $v_{\mathrm{A\,1\,O}}$ and $v_{\mathrm{A\,2\,O}}$ corresponding to frequency $m\omega_c + n\omega_0$ can be expressed as the following form:

$$v_{A_1O}(m,n)(t) = C_{mn}\cos[(m\omega_c + n\omega_0)t + m\theta_{c1} + n\theta_0 + \theta_{mn}] \tag{1}$$

$$v_{A_2O}(m,n)(t) = C_{mn}\cos[(m\omega_c + n\omega_0)t + m\theta_{c2} + n\theta_0 + \theta_{mn}] \tag{2}$$

where $C_{mn}$ is the harmonic amplitude; $\theta_c$ and $\theta_0$ are the initial angles of the carrier and reference waves, respectively; and $\theta_{mn}$ is a constant value, depending on the system operation condition.

By phase shifting the PWM switching sequence of individual inverter at a specific angle, the total voltage ripple due to PWM switching at the ac terminal can be reduced through selected harmonic-current cancellation or reduction. However, interleaving results in instantaneous voltage differences between two modules in the output side, thus producing the circulating current. It should be noted that because the fundamental component $v_{A1O}$ (0,1) is the same as $v_{A2O}$ (0,1), the amplitude of $v_{AO\_\mathrm{fundamental}}$ remains the same as $C_{01}$, i.e., (3). The fundamental differential voltage between two inverters in phase *A* is 0 as expressed in (4), so the circulation does not contain the fundamental component

$$\begin{aligned} v_{AO\_\mathrm{fundamental}} &= 0.5(v_{A_1O}(0,1) + v_{A_2O}(0,1)) \\ &= C_{01}\cos[\omega_0 t + \theta_0 + \theta_{01}] \end{aligned} \tag{3}$$

$$v_{A_1-A_2\_\mathrm{fundamental}} = v_{A_1O}(0,1) - v_{A_2O}(0,1) = 0. \tag{4}$$

Situation is different for harmonic components. Assuming an angle shift of $\theta_k$ by the VSI2 carrier, i.e., shown in (5), the amplitude of the output voltage $v_{AO\_\mathrm{harmonic}}$ is expressed in (6) and the differential voltage between two inverters $v_{AO\_\mathrm{differential}}$ is shown in (7)

$$\theta_{c2} = \theta_{c1} + \theta_k \tag{5}$$

$$\begin{aligned} v_{AO\_\mathrm{harmonic}} &= 0.5(v_{A1O}(m,n) + v_{A2O}(m,n)) \\ &= C_{mn}\cos(m\theta_k/2)\cos[(m\omega_c + n\omega_0)t \\ &\quad + m(\theta_{c1} + \theta_k/2) + n\theta_0 + \theta_{mn}] \end{aligned} \tag{6}$$

$$\begin{aligned} v_{AO\_\mathrm{differential}} &= 0.5(v_{A1O}(m,n) - v_{A2O}(m,n)) \\ &= C_{mn}\sin(m\theta_k/2)\sin[(m\omega_c + n\omega_0)t \\ &\quad + m(\theta_{c1} + \theta_k/2) + n\theta_0 + \theta_{mn}]. \end{aligned} \tag{7}$$

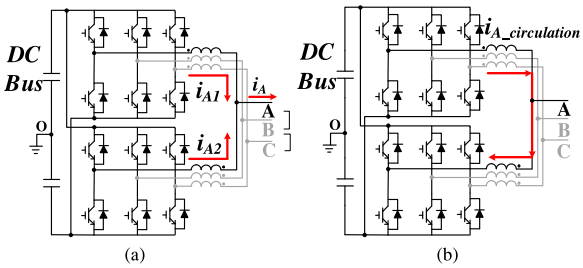


Fig. 3. Current-moving path in paralleled inverters with interleaving. (a) Output component. (b) Circulating component.

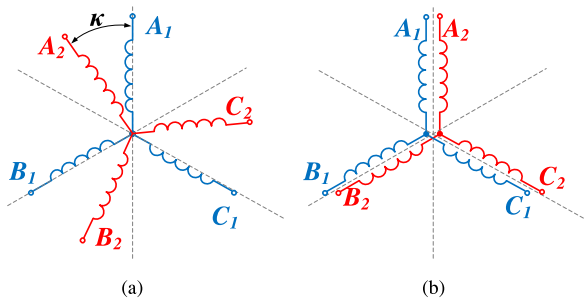


Fig. 4. Angle between the 2 three-phase sets: (a) conventional dual three-phase machine with a displacement ($0 < \kappa < \pi/3$) and (b) two-segment machine with no displacement ($\kappa = 0$).

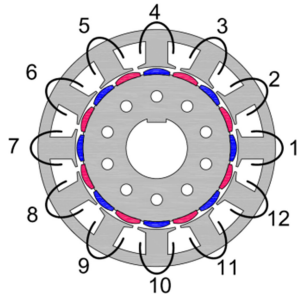


Fig. 5. Designed 0.9-kW, 12-slot, 16-pole PMSM topology.

In fact, the interleaving method to reduce ac-side current harmonics is achieved through utilizing differential voltage between $v_{A1O}$ and $v_{A2O}$. By setting $\theta_k$ as a specific value in (6), $\pi$, for instance, all odd-order switching-frequency harmonics in average voltage between $v_{A1O}$ and $v_{A2O}$ will disappear but turn up in the differential voltage counterpart. Therefore, these differential voltage harmonics in (7) will inevitably bring the circulating current between the two inverters. The current-moving path for the output component has been illustrated in Fig. 3(a); this current group mainly contains even switching frequency harmonics and their sidebands. The current-moving path for the differential component has been marked in Fig. 3(b); this mainly contains odd switching frequency harmonics and their sidebands. Generally, different specific order current harmonics will be eliminated in the ac side with different $\theta_k$, thus reducing the total harmonic distortion (THD) of the current. However, to prevent excessive circulation damaging switch, large inductors in ac side is indispensable. The value of inductors is designed according to the limit of peak circulation, and there are many papers concentrated on the inductors type [16], [17]. Nevertheless, no matter which inductors are selected, they will bring extra hardware to the drive system, thus increasing the system weight and volume. In addition, although the circulation is suppressed, it still exists between two modules, decreasing system efficiency.

### B. Proposed Two-Segment PMSM

In ac machine winding theory, the concept of unit machine is used to describe the machine's minimum electromagnetic active part. Essentially, an ac electrical machine can be regarded as a combination of multiple repeating unit machines. The electrical periodicity $t$, defined as the greatest common divisor between the slot number $Z$ and the pole pair number $p$, i.e., $t = \mathrm{GCD}\{Z, p\}$, is commonly used to represent the number of unit machines involved in a whole machine. Obviously, $t$ equals the maximal value of achievable winding segment number.

Using the concept of unit machine, a multisegment machine is developed. Each segment has been designed corresponding to a unit machine. Based on this design, machine electrical ports number will be doubled or even more, and paralleling inverters are no longer necessary in this machine type. Because each module is connected independently with others, it can be controlled individually and the circulation path between modules that exist in the paralleled inverters will disappear. Thus, output inductors are removed, and the volume of the drive system is decreased; correspondingly, power density and efficiency are improved.

The winding arrangement for a multisegment machine is an important part for the machine performance. A typical two-segment machine is a dual three-phase machine [14], with two groups of windings. For the dual three-phase machine, the three-phase sets are shifted by the angle $\kappa(0 < \kappa < \pi/3)$ to suppress back-EMF low-frequency harmonics, shown in Fig. 4(a). However, the winding phase shift will bring the different fundamental current in two groups of windings and make the control to be complex for torque ripple reduction. Different from conventional dual three-phase machine, the electrical angle of two sets windings in a two-segment machine has been kept the same, as it shows in Fig. 4(b). In order to avoid the magnetic circuit coupling between modules, as mentioned in [19] and [20], the two sets windings are placed in different slots in two semicircles in the stator. As a low-power prototype for performance verification, the $d$- and $q$-inductances are relatively small. But back EMF will be kept with the same phase for two groups of windings.

In order to develop the phase-shift PWM method for two-segment machine and validate the result, a prototype machine has been designed. As shown in Fig. 5, a 0.9-kW, 12-slot, 16-pole PMSM with double-layer windings has been designed to serve as a two-segment machine. The star of slots for the 12 coils is illustrated in Fig. 6, with each phase sharing four identical slot vectors. For the PMSM system in this paper, the two-segment winding is adopted by configuring connection of 12 coils, as shown in Fig. 7. It should be noted that there is no electrical connection between the two winding segments. Some key parameters of the designed machine are listed in Table I.

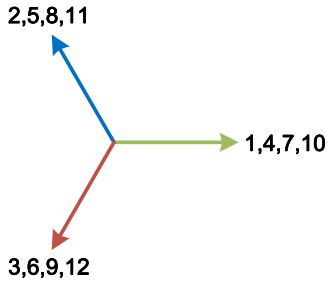


Fig. 6. Star of slots for 12/16 combination.

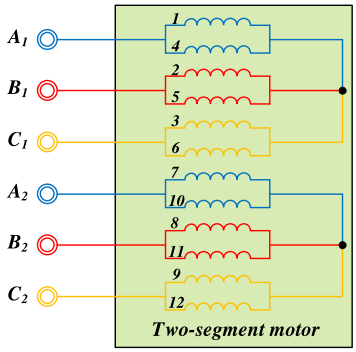


Fig. 7. Winding connection of the 12 coils.

TABLE I
KEY PARAMETERS OF THE DESIGNED PMSM

| Item | Item |
|---|---|
| PM flux linkage | 0.023 Wb |
| *d*-axis inductance | 0.45 mH |
| *q*-axis inductance | 0.45 mH |
| Phase resistance | 0.2 Ω |
| Rated rotation speed | 1000 rpm |
| Rated line voltage | 37.5 V |
| Rated line current | 17 A |
| Rated torque | 8.3 Nm |
| DC link voltage | 75 V |

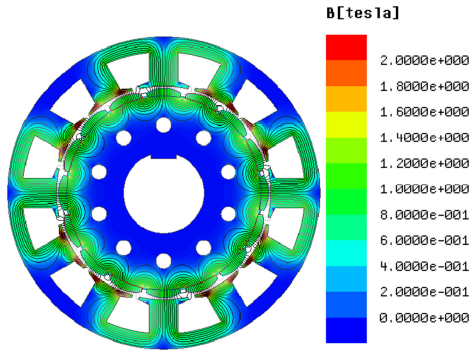


Fig. 8. Flux contour plot of the designed machine.

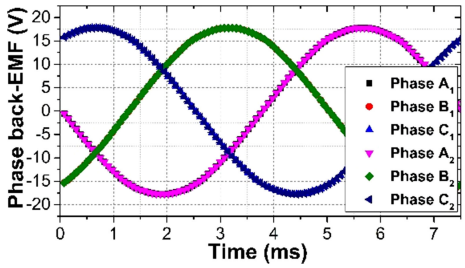


Fig. 9. Back-EMF waveforms of the six-phase windings.

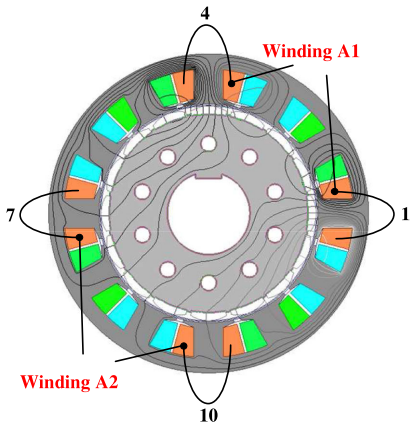


Fig. 10. Armature reaction of the winding A1.

The no-load flux contour plot of the designed machine is calculated through finite-element analysis (FEA) and shown in Fig. 8. From the flux distribution in the stator part, it can be clearly seen that the electrical periodicity $t = 4$. The back EMF of the six-phase windings are shown in Fig. 9, and the corresponding phases are with exactly the same real-time waveforms. Hence, the volt–second characteristic of the two VSIs should remain the same in any subcycle, and the fundamental voltage and current waveforms of any two corresponding phases (e.g., A1 and A2) should remain exactly the same, respectively. Fig. 10 shows the flux distribution of the machine when phase A1 is fed with the rated current and A2 keeps in open-circuit condition. From the picture, it can be seen that there is only weak magnetic coupling between A1 and A2 and the mutual inductance is thereby much lower than the self-inductance. The numerical FEA result shows that the self-inductance is 0.293 mH and the mutual inductance between A1 and A2 is 0.0343 mH, only ∼11% that of self-inductance, which indicates that the cross-coupling effect between the two modules can be neglected. The windings of two segments can be controlled independently and only coupled in the electromagnetic torque in the rotor. This is the basis of the proposed control method.

Moreover, the rotor skewing and the magnet shape optimization have been applied to minimize the cogging torque and torque ripple in the machine design process. Fig. 11 shows the cogging and torque ripple waveforms under rated current, from which it can be seen that the peak-to-peak value of torque ripple has been reduced to ∼0.09 N·m when the machine is fed with pure sinusoidal phase current. The carrier phase-shift method is to deal with the torque ripple caused by the switching current ripple, which is apart from the torque ripple caused by the machine itself. With this prototype machine, the torque ripple and vibration reduction effect caused by carrier phase-shift method can be seen more clearly.

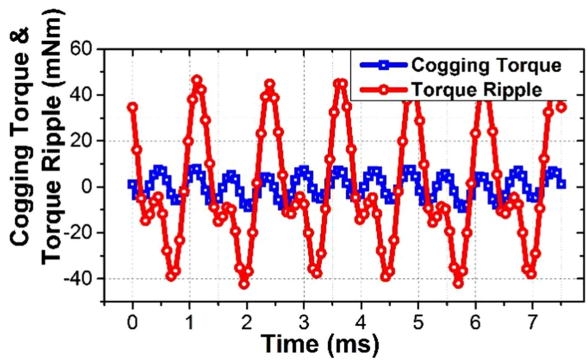


Fig. 11. Cogging torque and torque ripple waveforms.

## III. Phase-Shift PWM for the Two-Segment Motor Drive

Based on the proposed two-segment machine in Section II, the torque-ripple-reduction-oriented phase-shift PWM method is analyzed and developed in this section.

### A. PMSM High-Frequency Vibration Analysis

Generally, the high-frequency electromagnetic vibration in PMSM can be divided into radial and tangential vibration, respectively. They are caused by the fluctuation of the radial electromagnetic force and tangential electromagnetic force in the motor. The tangential force is determined by electromagnetic torque of the machine, which is well formulated with current. Apart from the tangential force, the radial electromagnetic force is also impacting the vibration of the machine and may be with even bigger effect and be the main source of motor vibration. The following section will focus on the analysis of radial electromagnetic vibration.

To analyze vibration, it is necessary to start from the air gap magnetic field since the air gap magnetic field is the medium of electromagnetic force. As mentioned in [21], air gap flux density is a function of changing space position $\theta$ and time $t$, which can be regarded as the sum of two parts (8): one is $B_{\mathrm{PM}}$, represents the flux density generated by PM; the other is $B_{\mathrm{winding}}$, represents the flux density generated by the machine stator winding current

$$B_{\mathrm{air\_gap}}(\theta,t) = B_{\mathrm{PM}}(\theta,t) + B_{\mathrm{winding}}(\theta,t). \tag{8}$$

Ignoring the saturation condition, the flux density can be expressed as the product of the air gap MMF $f_{\mathrm{air\_gap}}(\theta,t)$ and the air gap permeance $\lambda(\theta, t)$

$$B_{\mathrm{air\_gap}}(\theta,t) = f_{\mathrm{air\_gap}}(\theta,t)\lambda(\theta,t). \tag{9}$$

Considering the factors of stator slotting and supposing the rotor surface is smooth, the air gap permeance can be written as (10), where $\Lambda_0$ is the average permeance amplitude of $\delta$ air gap length, $\Lambda_k$ is the amplitude of $k$-order harmonic permeance, and $Z_1$ is the stator slot number

$$\lambda(\theta,t) = \Lambda_0 + \sum_{k=1}^{\infty} \Lambda_k \cos(kZ_1\theta). \tag{10}$$

When the machine is driven by a PWM inverter, the air gap MMF is divided into three parts in (11): $f(\theta, t)$ is the magnetomotive force contributed by rotor PM, $f_\nu(\theta,t)$ is contributed by the fundamental current of stator winding, and $f_h(\theta,t)$ is contributed by high-frequency harmonic current [22]. The subscript $\nu$ means the harmonic orders of armature winding field and $h$ means the harmonic orders of high-frequency current ripple

$$f_{\mathrm{air\_gap}}(\theta,t) = f(\theta,t) + \sum f_v(\theta,t) + \sum f_h(\theta,t). \tag{11}$$

Further, the air gap MMF can be expressed as the following form:

$$f_{\mathrm{air\_gap}}(\theta,t) = \sum_{\mu} F_\mu \cos(\mu\omega_1 t - \mu\theta + \varphi_1) + \sum_{\nu} F_\nu \cos(\omega_1 t - \nu\theta + \varphi_2) + \sum_{h}\sum_{\nu} F_h \cos(h\omega_1 t - \nu\theta + \varphi_3) \tag{12}$$

where $F_\mu$ represents the $\mu$-order MMF amplitude contributed by rotor PM, $F_\nu$ is the $\nu$-order MMF amplitude contributed by the fundamental current of stator winding, and $F_h$ is the $h$-order MMF amplitude contributed by high-frequency harmonic current. $p$ is the number of pole pairs of the machine and $\varphi_1$, $\varphi_2$, and $\varphi_3$ are the initial phases.

Substituting (10) and (12) into (9), the air gap flux density is obtained as

$$\begin{aligned} B_{\mathrm{air\_gap}}(\theta,t) = {} & \sum_{\mu} F_\mu \Lambda_0 \cos(\mu\omega_1 t - \mu\theta + \varphi_1) \\ & + \sum_{\nu} F_\nu \Lambda_0 \cos(\omega_1 t - \nu\theta + \varphi_2) \\ & + \sum_{h}\sum_{\nu} F_h \Lambda_0 \cos(h\omega_1 t - \nu\theta + \varphi_3) \\ & + \sum_{\mu}\sum_{k} \frac{1}{2} F_\mu \Lambda_k \cos[\mu\omega_1 t - (\mu \pm kZ_1)\theta + \varphi_1] \\ & + \sum_{\nu}\sum_{k} \frac{1}{2} F_\nu \Lambda_k \cos[\omega_1 t - (\nu \pm kZ_1)\theta + \varphi_2] \\ & + \sum_{h}\sum_{\nu}\sum_{k} \frac{1}{2} F_h \Lambda_k \cos[h\omega_1 t - (\nu \pm kZ_1)\theta + \varphi_3]. \end{aligned} \tag{13}$$

According to the Maxwell stress equation, the analytic formula of the radial electromagnetic force $p_{\mathrm{r}}$ in the air gap of PMSM can be expressed as

$$p_r \approx \frac{B^2{}_{\mathrm{air\_gap}}(\theta,t)}{2\mu_0}. \tag{14}$$

The formula expansion is very complicated, which is not listed here. The interactions between the high-frequency harmonic current field and field of the PM, the high-frequency harmonic current field and fundamental magnetic field of armature current are primary components of $p_{\mathrm{r}}$. The frequency of these electromagnetic force harmonics is mainly concentrated on the switching frequency and its multiples. The cancellation

of torque harmonics is associated with the cancellation of radial force and thus reducing the machine vibration together.

### *B. Torque Ripple Analysis and Reduction*

Like the conventional paralleled drive system, the output phase voltage of two-segment motor drive system is expressed as (1) and (2) according to the double-integral Fourier analysis. Correspondingly, the analytical formula for three-phase output current can be derived as (15), (16), and (17), where $C'_{mn}$ is the harmonic current amplitude, $\varphi$ is the power factor angle. It can be seen that since the phase voltage contains components of carrier-wave frequency harmonics, and, in turn, these frequency harmonics will result in three-phase current harmonics. In fact, these $(m\omega_c + n\omega_0)$ order current harmonics contribute greatly to high-frequency vibration noise. Through current harmonics components analysis in PMSM drive with SVPWM modulation strategy, it can be concluded that the main phase current harmonics concentrate on the first and the second switching frequency and their sidebands

$$i_{A1}(m,n)(t) = C'_{mn}\cos[(m\omega_c + n\omega_0)t + m\theta_c + n\theta_0 + \theta_{mn} + \varphi] \tag{15}$$

$$i_{B1}(m,n)(t) = C'_{mn}\cos\left[(m\omega_c + n\omega_0)t + m\theta_c + n\left(\theta_0 - \frac{2}{3}\pi\right) + \theta_{mn} + \varphi\right] \tag{16}$$

$$i_{C1}(m,n)(t) = C'_{mn}\cos\left[(m\omega_c + n\omega_0)t + m\theta_c + n\left(\theta_0 + \frac{2}{3}\pi\right) + \theta_{mn} + \varphi\right]. \tag{17}$$

With the linear model of PMSM, the high-frequency torque ripple expression can be determined. First, the three-phase current harmonics can be turned into rotor reference frame by Park transformation (18), where $\theta_e$ is the rotor position. Then, the torque ripple in the surface-mounted PMSM is deducted as (19), where $\Psi_f$ is the flux linkage produced by PMs

$$\begin{pmatrix} i_d(m,n)(t) \\ i_q(m,n)(t) \end{pmatrix} = \frac{2}{3}\begin{pmatrix} \cos\theta_e & \cos\left(\theta_e - \frac{2}{3}\pi\right) & \cos\left(\theta_e + \frac{2}{3}\pi\right) \\ -\sin\theta_e & -\sin\left(\theta_e - \frac{2}{3}\pi\right) & -\sin\left(\theta_e + \frac{2}{3}\pi\right) \end{pmatrix} \times \begin{pmatrix} i_A(m,n)(t) \\ i_B(m,n)(t) \\ i_C(m,n)(t) \end{pmatrix} \tag{18}$$

$$T_e = \frac{3}{2}p\psi_f i_q = \mp\frac{3}{2}p\psi_f \cdot C'_{mn}\sin[(m\omega_c + n\omega_0)t + m\theta_c + n\theta_0 + \theta_{mn} + \varphi \pm \theta_e]. \tag{19}$$

The amplitude of switching frequency current ripple is generally dominated by both modulation ratio and torque angle,

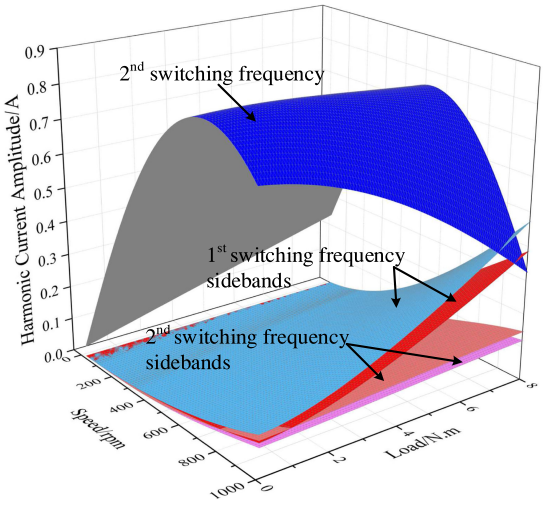


Fig. 12. Harmonic current calculation result in the full operation range.

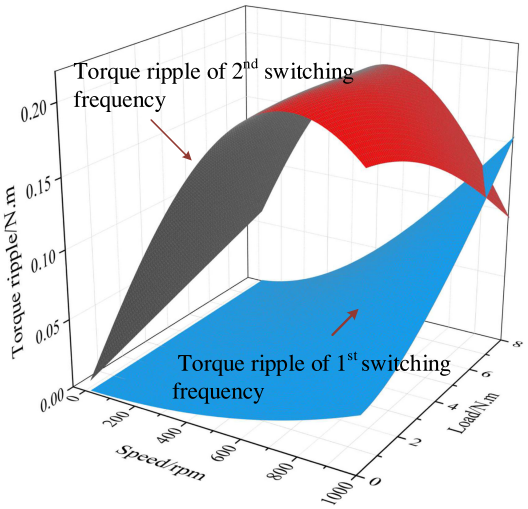


Fig. 13. Torque ripple result in the full operation range.

which are further determined by motor speed and load condition. The curved surfaces of the $q$-axis harmonic current versus motor speed and load, calculated from the double-integral Fourier analysis, are illustrated in Fig. 12, along with the torque ripple illustrated in Fig. 13. It can be seen that both the main component of $q$-axis current and the torque ripple harmonics in rotor frame concentrate on the second switching frequency harmonics and its sidebands. Therefore, the main target of torque ripple reduction is second switching frequency harmonics.

For the two-segment motor mentioned before, when control instruction for the two inverters are the same, the terminal phase current for the two groups of windings will also be the same, including the fundamental and switching harmonics. In that case, the torque harmonics generated in two segments will be the same and the total torque ripple are these two parts added as a scalar function, similar to conventional PMSM. However, inspired by interleaving method in paralleled inverters, if one of the two inverters carrier phase is shifted by an angle $\Delta\theta = 2\pi/4$,

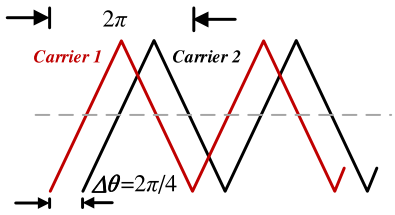


Fig. 14. Carrier-wave phase shift.

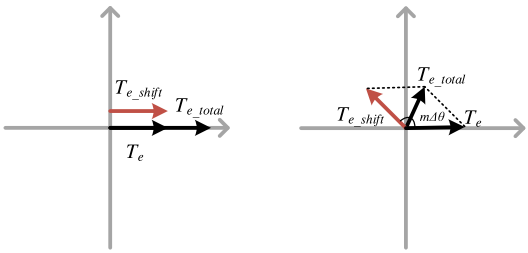


Fig. 15. Total torque harmonics (two-order switching frequency). (a) Without carrier phase shift. (b) With carrier phase shift.

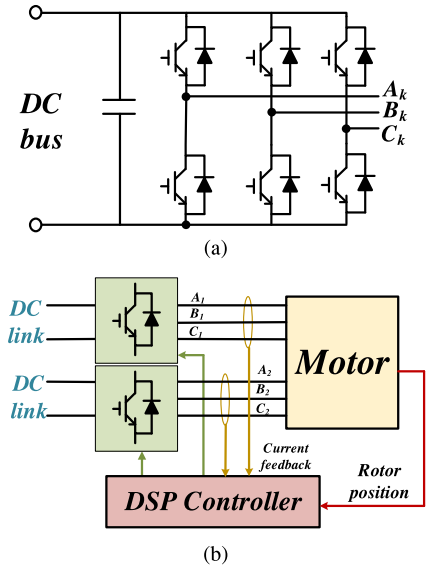


Fig. 16. Two-segment motor drive architecture. (a) Single unit. (b) Full system.

as shown in the Fig. 14, the corresponding phase output voltage and current harmonic of this inverter will have a phase shift $m \cdot \Delta\theta$ in the initial phase term compared to the nonshift one. The expression of phase voltage, current, and torque are rewritten from (20) to (23). As a result, the amplitudes of second switching frequency torque harmonics generated by two segments, respectively, remain the same but phase is shifted $\pi$ exactly, which is shown in Fig. 15. By vector summation (23), the second switching frequency harmonic and its sidebands in the total torque ripple will be eliminated completely and other order harmonics will also have an attenuation simultaneously, thus greatly smoothing the output torque. Similarly, the radial magnetic force will also have this kind of cancellation of harmonics and improve the vibration together with the reduction of torque harmonics

$$v'_{AO}(m,n)(t) = C_{mn}\cos[(m\omega_c + n\omega_0)t + m(\theta_c + \Delta\theta) + n\theta_0 + \theta_{mn}] \quad (20)$$

$$i_A(m,n)(t) = C'_{mn}\cos[(m\omega_c + n\omega_0)t + m(\theta_c + \Delta\theta) + n\theta_0 + \theta_{mn} + \varphi] \quad (21)$$

$$T_{e\_\text{shift}} = \frac{3}{2}p\psi_f \cdot C'_{mn}\sin[(m\omega_c + n\omega_0)t + m(\theta_c + \Delta\theta) + n\theta_0 + \theta_{mn} + \varphi \pm \theta_e] \quad (22)$$

$$T_{e\_\text{total}} = T_e + T_{e\_\text{shift}}. \quad (23)$$

### C. Drive System Structure

The single unit of drive system structure is shown in Fig. 16(a), which is with normal three-phase VSI structure. The full system is depicted in Fig. 16(b). The motor is driven by two drive units to generate the required torque. Each group of windings is excited independently with symmetrical three-phase voltage by VSI. Clearly, ignoring the magnetic coupling between two sets of windings, the mathematical model of each unit machine is identical with a regular PM machine. The *d–q* axis flux and voltage equations in the rotor reference frame can be written as (24) and (25)

$$\begin{bmatrix}\psi_{dk}\\ \psi_{qk}\end{bmatrix} = \begin{bmatrix}L_{dk} & 0\\ 0 & L_{qk}\end{bmatrix}\begin{bmatrix}i_{dk}\\ i_{qk}\end{bmatrix} + \begin{bmatrix}\psi_f\\ 0\end{bmatrix} \quad (24)$$

$$\begin{bmatrix}U_{dk}\\ U_{qk}\end{bmatrix} = \begin{bmatrix}R_s & 0\\ 0 & R_s\end{bmatrix}\begin{bmatrix}i_{dk}\\ i_{qk}\end{bmatrix} + \begin{bmatrix}d\psi_{dk}/dt\\ d\psi_{qk}/dt\end{bmatrix} + \begin{bmatrix}-\omega_r\psi_{qk}\\ \omega_r\psi_{dk}\end{bmatrix} \quad (25)$$

where the subscript $k$ stands for any unit of the machine (e.g., $k = 1,2$), $\Psi_{dk}$, $\Psi_{qk}$, $i_{dk}$, $i_{qk}$, $U_{dk}$, and $U_{qk}$ are the *d–q* axis flux linkages, currents, and voltages, respectively. $R_s$ is the resistance per phase. $\omega_r$ stands for the electrical angular speed of the rotor.

Since the prototype machine is designed as surface mounted PMSM, in this paper, $i_d = 0$ vector control strategy is adopted. The whole control block diagram is shown in Fig. 17. It is with one speed controller in the outer loop and two current controllers in the inner loop. Speed controller gives $q$-axis current reference in the rotor reference frame and is divided equally into two parts as the current references of each unit controller input. Two current controllers work independently to generate the three-phase voltage duty cycle of the corresponding phase.

It should be noted that for the major second-order harmonics torque ripple cancellation, carrier-wave phase has been shifted with $0.25T_s$, as shown in Fig. 18. The switching signal can be obtained through the comparison between the duty cycle and

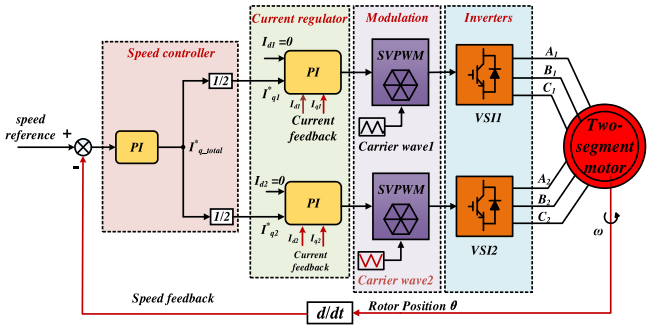


Fig. 17. Controller structure for the two-segment motor drive.

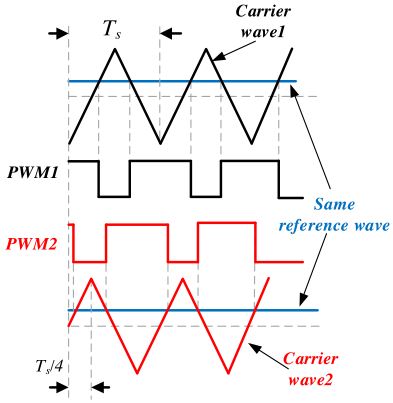


Fig. 18. Carrier-wave phase shift with $T_s/4$.

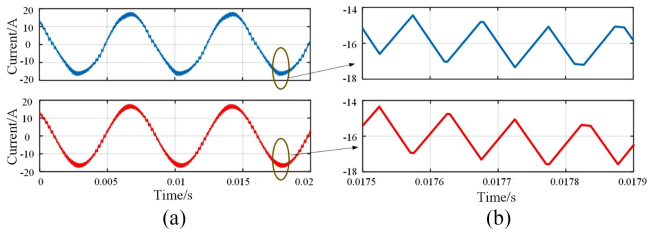


Fig. 19. Each unit A phase current ripple: simulation results.

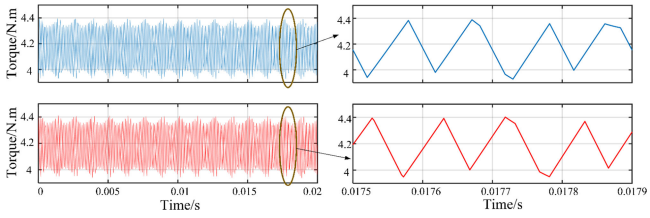


Fig. 20. Each unit torque ripple: simulation results.

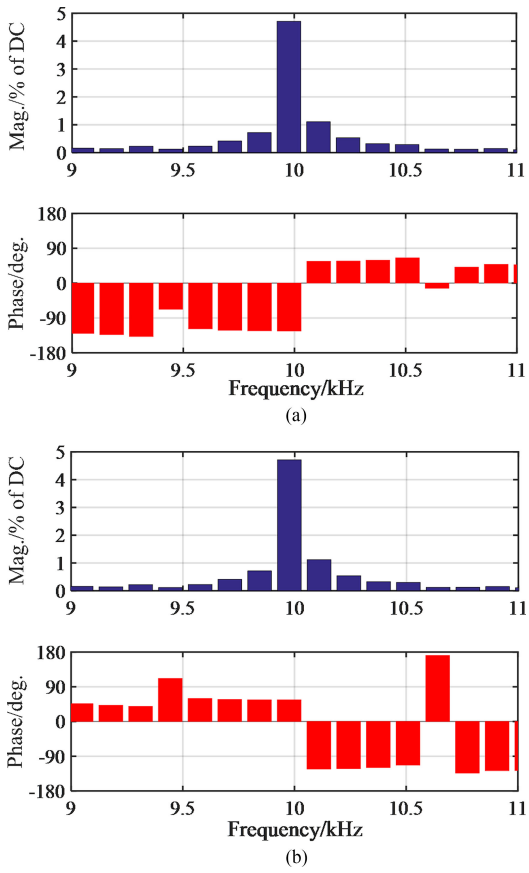


Fig. 21. FFT analysis of torque ripple in two switching cycles with phase shift. (a) Unit 1. (b) Unit 2.

the carrier. Then these phase-shifted switching signals are given to two inverters to drive the motor.

## IV. Simulation Results

Based on the derived model of a two-segment motor in Section III, a simulation model of a two-segment motor has been developed in Simulink, with $i_d = 0$ vector control strategy and PWM phase-shift modulation method. The motor is driven by two converters with 5 kHz switching frequency.

Figs. 19 and 20 show the contrast of current and torque ripple produced by two units, respectively, in two switching cycles. It is obvious that the current ripples of two inverters are nearly out of phase and hence result in the torque ripples nearly out of phase. Fast Fourier transform (FFT) analysis of torque ripple has been done in Fig. 21 for the two units, with both amplitude and phase. It can be verified that the major component of the torque harmonics is the second-order harmonic of switching frequency (10 kHz) for either of the unit. With the proposed phase-shift PWM, the 10-kHz torque amplitudes of the two units are nearly the same, approximately 5% of the average torque (dc value). However, the phases for the torque component in two units are 180° shifted at 10 kHz, which are −120° in unit 1 and 60° in unit 2. Adding them together, the 10 kHz components are opposite with each other. Fig. 22 shows the total torque harmonics for the case before and after phase shift. When there is no phase shift in PWM, the 10-kHz torque components in two units will be with the same phase and amplitude and the total torque harmonic is about 5% of the average torque. With the proposed phase shift, the 10-kHz torque components in two units will be of the same amplitude but opposite phase, and the total torque harmonic is nearly zero. Consequently, the total torque ripple at 10 kHz will be cancelled in comparison with the case before phase shift and other frequency harmonics will have a decrease too.

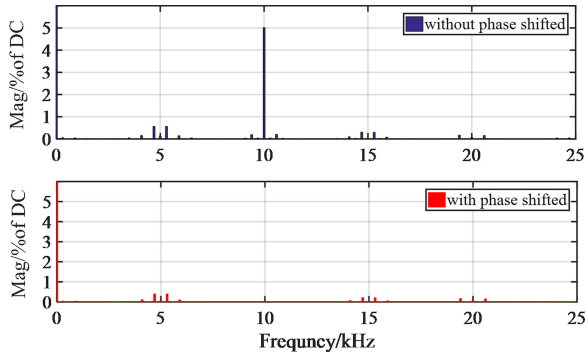


Fig. 22. FFT analysis of total torque before and after carrier phase shift: simulation results.

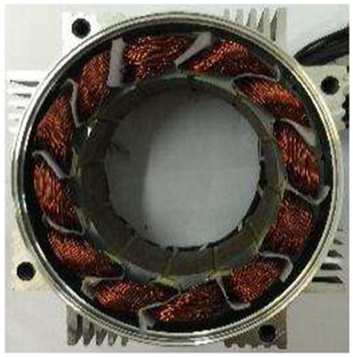

Fig. 23. Stator of the prototype.

Fig. 24. Rotor of the prototype.

## V. Hardware and Experiments

According to the optimal designed PMSM topology, a prototype PMSM with two segments has been fabricated, with the stator and rotor shown in Figs. 23 and 24, respectively. It can be seen from Fig. 24 that a two-segment rotor skewing has been adopted to reduce the cogging torque and torque ripple from the standpoint of machine design. To validate the forgoing analysis, experiment has been done based on DSP of TMS320F28335 from Texas Instrument and two integrated power-module-based converter. The experimental platform is shown in Fig. 25. The motor is driven with 5 kHz switching frequency at 0.6 of the rated speed and load.

Fig. 26 shows the phase current between two units, including the full-scale and enlarged details in few switching cycles. In

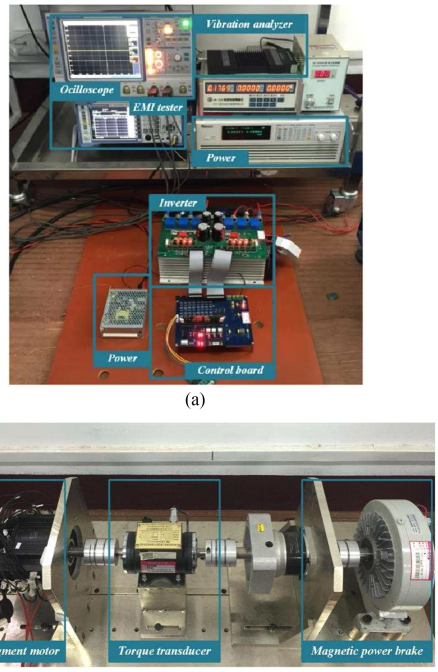


Fig. 25. Experimental platform. (a) Drive system of the machine. (b) Test bench.

Fig. 26(a), when carrier phase has not been shifted, current ripple in two units are nearly the same. But in Fig. 26(b), when carrier phase has been shifted, current ripple in two units are close to each other, validating the assumption that the two units share the same current and average torque. With the enlarged details, it can be seen that current harmonics phases have been shifted by 1/4 of the switching cycle. Because the major component of the current harmonic is the second order of switching frequency, the current ripple in two units is close to opposite values.

Contrast of electromagnetic torque ripple before and after carrier-wave phase shifting is illustrated in Fig. 27. It is clear that the average torques before and after phase shifted are nearly the same but the high frequency torque ripple after phase shifted is significantly reduced by less than 20% of the case before phase shifted. To further prove the effectiveness of the carrier-wave phase shift method, EMI test of the dc bus current has been done with Rohde & Schwarz EMI analyzer. The test result is illustrated in Fig. 28, which shows the noise of switching has been greatly attenuated after carrier-wave phase shift, which is similar with the paralleled inverters with interleaving.

FFT analysis of torque ripple is shown in Fig. 29. Without carrier phase shift, the main torque harmonic is the second-order harmonic of the switching frequency, which is with 6% of the rated torque value. With carrier-wave phase shift, the main harmonic of torque ripple, which is concentrated around the second order of switching frequency, is nearly eliminated and the whole torque ripple is decreased by 6% of the rated torque. To further validate the benefit for vibration and noise, motor vibration test has been done by vibration facility of Pulse Labshop from Bruel&Kjar. Experimental results are shown in Fig. 30. The vibration parameters are also dominated by the

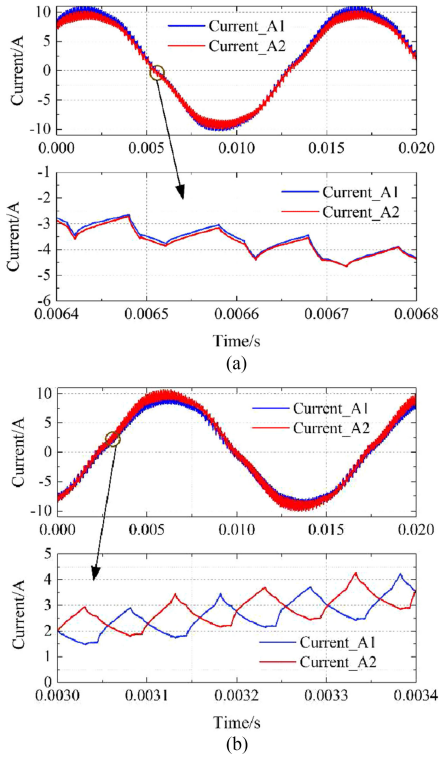


Fig. 26. Contrast of current ripple between two units. (a) Without phase shift. (b) With phase shift.

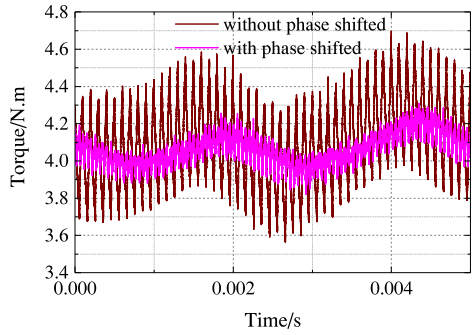


Fig. 27. Comparison of electromagnetic torque.

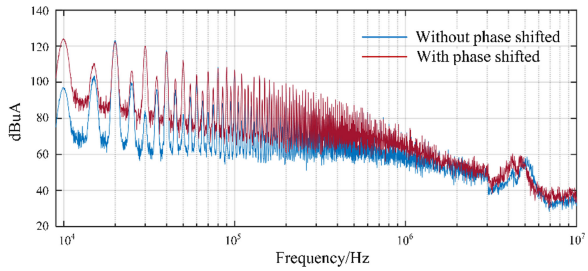


Fig. 28. EMI test of dc-bus current: without phase shift and with phase shift.

components near 10 kHz when there is no carrier phase shift. With carrier-wave phase shift, the vibration amplitude near 10 kHz has been significantly reduced and the noise of the drive system has been also improved obviously.

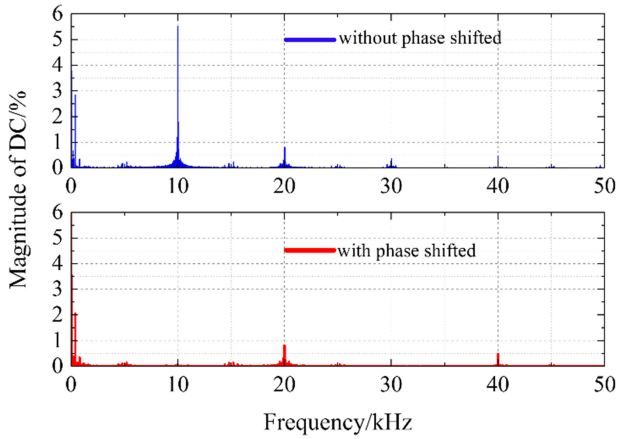


Fig. 29. FFT analysis of torque ripple.

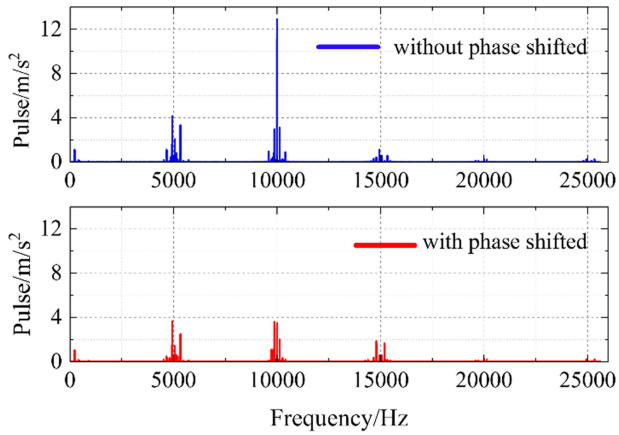


Fig. 30. FFT analysis of vibration.

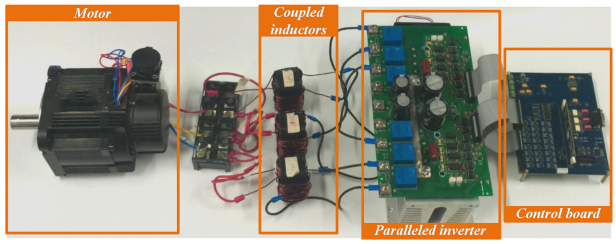


Fig. 31. Connection of paralleled inverters with coupled inductors to the motor with regular three-phase winding: for comparison.

To illustrate the superiority of the method mentioned earlier, an experiment of an equivalent regular three-phase PM machine driven by two paralleled inverters has been conducted for comparison. The machine is with the same rotor and stator with the two segments machine in Figs. 23 and 24. But the winding connection is to form a regular three-phase PM machine. It should be noted that to reduce the phase current harmonics, the phase-shift PWM method has been applied here and the switching sequence of the two inverters are differing from each other. Therefore, coupled inductors are needed to inhibit the circulating current between different inverters. Fig. 31 shows the connection of paralleled inverters, coupled inductors, and motor for comparing experiments. The value of the inductance

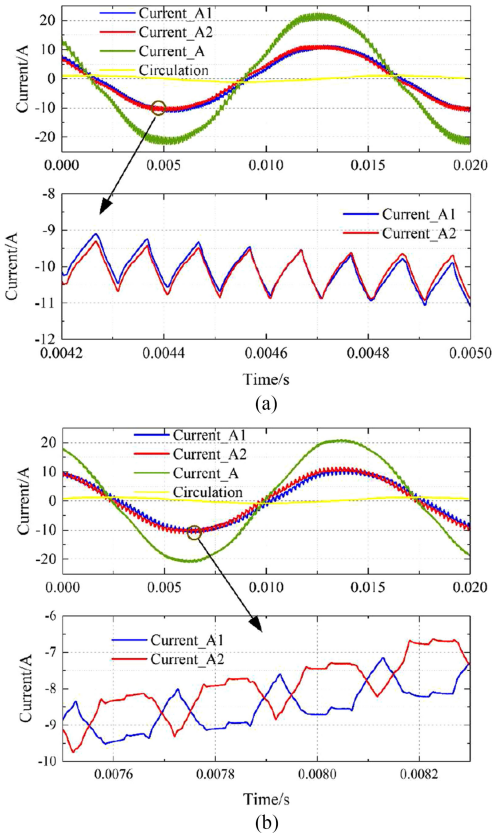


Fig. 32. Current waveform between two blocks for paralleling inverters. (a) Without interleaving. (b) With interleaving.

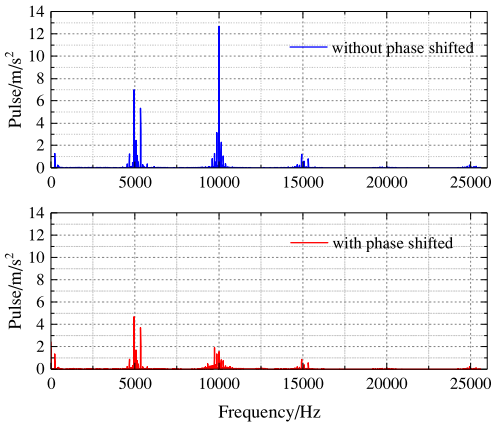


Fig. 33. FFT analysis of vibration.

determines the peak value of the circulating current. In this experiment, the circulating current is suppressed by less than 10% of the phase output current peak value. The motor is also driven with 5 kHz switching frequency at 0.6 of the rated speed and load. Compared with the architecture in Fig. 25, three extra coupled inductors are needed for the setup in Fig. 31.

From the experimental results in Fig. 32, the circulation is suppressed to less than 8% of the phase current peak value. Vibration test results are shown in Fig. 33. Similar to the vibration results in Fig. 30, with carrier phase shift, the vibration amplitude near 10 kHz has been significantly reduced. From experimental results, a two-segment motor can suppress high-frequency vibration while saving three coupled interface inductors compared to paralleling inverters method. The power density and efficiency are improved.

## VI. Conclusion

Two-segment motor system can meet the requirement of high power and reduce torque ripple simultaneously. This paper gives a study of this motor and its drive system. Based on the operation principle of the two-segment motor system, the precise theory of torque ripple reduction of this motor is developed. Then, the control strategy of this machine is illustrated together with simulation and experimental results for validation. Here, few conclusions can be derived:

1) With the two-segment motor, it can be driven by two regular inverters to equally share the average torque and power.
2) By adjusting the phase-shift angle between the carriers in two inverters, certain torque ripple can be theoretically cancelled for the whole drive system.
3) With the simulation of full operation of the prototype, it can be determined that the dominating torque harmonic is near the second order of switching frequency. By phase shifting of 1/4 of the switching cycle in the carrier, this component can be significantly reduced.
4) Simulation and experiment have been completed with a prototype motor drive system. The FFT analysis of torque ripple and online vibration test results have validated this method effectiveness.
5) Compared with conventional three-phase machine driven by paralleled inverters with phase-shift PWM, the torque ripple reduction capability of the two-segment motor with phase-shift PWM is similar. But for the proposed two-segment machine, there is very little coupling between two inverters and no coupled inductors are needed for circulating current control, the system power density is increased, and cost is reduced greatly. It can be a good candidate for electrical propulsion technology.

## References

[1] S. Chen, C. Namuduri, and S. Mir, "Controller-induced parasitic torque ripples in a PM synchronous motor," *IEEE Trans. Ind. Appl.*, vol. 38, no. 5, pp. 1273–1281, Nov. 2012.
[2] Z. Azar, Z. Q. Zhu, and G. Ombach, "Influence of electric loading and magnetic saturation on cogging torque, back-EMF and torque ripple of PM machines," *IEEE Trans. Magn.*, vol. 48, no. 10, pp. 2650–2658, Oct. 2016.
[3] J. W. Kimball and M. Zawodniok, "Reducing common-mode voltage in three-phase sine-triangle pwm with interleaved carriers," *IEEE Trans. Power Electron.*, vol. 26, no. 8, pp. 2229–2236, Aug. 2011.
[4] W. Liang, J. Wang, P. C. K. Luk, W. Fang, and W. Fei, "Analytical modeling of current harmonic components in PMSM drive with voltage-source inverter by SVPWM technique," *IEEE Trans. Energy Convers.*, vol. 29, no. 3, pp. 673–680, Sep. 2014.
[5] K. Basu, J. S. S. Prasad, and G. Narayanan, "Minimization of torque ripple in PWM AC drives," *IEEE Trans. Ind. Electron.*, vol. 56, no. 2, pp. 553–558, Feb. 2009.
[6] K. Taniguchi, M. Inoue, Y. Takeda, and S. Morimoto, "A PWM strategy for reducing torque-ripple in inverter-fed induction motor," *IEEE Trans. Ind. Appl.*, vol. 30, no. 1, pp. 71–77, Jan./Feb. 1994.

[7] E. Jung, H. Yoo, S. K. Sul, H. S. Choi, and Y. Y. Choi, "A nine-phase permanent-magnet motor drive system for an ultrahigh-speed elevator," *IEEE Trans. Ind. Appl.*, vol. 48, no. 3, pp. 987–995, May/Jun. 2012
[8] D. J. Perreault and J. G. Kassakian, "Distributed interleaving of paralleled power converters," *IEEE Trans. Circuits Syst. I, Fundam. Theory Appl.*, vol. 44, no. 8, pp. 728–734, Aug. 1997.
[9] K. Xing, F. C. Lee, D. Borojevic, Z. Ye, and S. Mazumder, "Interleaved PWM with discontinuous space-vector modulation," *IEEE Trans. Power Electron.*, vol. 14, no. 5, pp. 906–917, Sep. 1999.
[10] L. Asiminoaei, E. Aeloiza, P. N. Enjeti, and F. Blaabjerg, "Shunt active-power-filter topology based on parallel interleaved inverters," *IEEE Trans. Ind. Electron.*, vol. 55, no. 3, pp. 1175–1189, Mar. 2008.
[11] D. Zhang, F. Wang, R. Burgos, R. Lai, and D. Boroyevich, "Impact of interleaving on AC passive components of paralleled three-phase voltage-source converters," *IEEE Trans. Ind. Appl.*, vol. 46, no. 3, pp. 1042–1054, May/Jun. 2010.
[12] D. Glose and R. Kennel, "Carrier-based pulse width modulation for symmetrical six-phase drives," *IEEE Trans. Power Electron.*, vol. 30, no. 12, pp. 6873–6882, Dec. 2015.
[13] D. Glose and R. Kennel, "Continuous space vector modulation for symmetrical six-phase drives," *IEEE Trans. Power Electron.*, vol. 31, no. 5, pp. 3837–3848, May 2016.
[14] Y. Miyama, M. Ishizuka, H. Kometani, and K. Akatsu, "Vibration reduction by applying carrier phase-shift PWM on dual three-phase windings permanent-magnet synchronous motor," *Proc. 2017 IEEE Int. Electr. Mach. Drives Conf.*, Miami, FL, USA, 2017, pp. 1–6.
[15] D. G. Holmes and T. A. Lipo, *Pulse Width Modulation for Power Converters—Principle and Practice*. New York, NY, USA: Wiley-IEEE Press, 2003, p. 219.
[16] L. Asimmoaei *et al.*, "An interleaved active power filter with reduced size of passive components," in *Proc. 21st Annu. IEEE Appl. Power Electron. Conf. Expo.*, Dallas, TX, USA, 2006, pp. 969–976.
[17] D. Wu, G. Calderon-Lopez, and A. J. Forsyth, "Discontinuous conduction/current mode analysis of dual interleaved buck and boost converters with interphase transformer," *IET Power Electron.*, vol. 9, no. 1, pp. 31–41, 2016.
[18] D. Zhang, F. Wang, R. Burgos, and D. Boroyevich, "Total flux minimization control for integrated inter-phase inductors in paralleled, interleaved three-phase two-level voltage-source converters with discontinuous space-vector modulation," *IEEE Trans. Power Electron.*, vol. 27, no. 4, pp. 1679–1688, Apr. 2012.
[19] M. Barcaro, N. Bianchi, and F. Magnussen, "Faulty operations of a PM fractional-slot machine with a dual three-phase winding," *IEEE Trans. Ind. Electron.*, vol. 58, no. 9, pp. 3825–3832, Sep. 2011.
[20] Y. Demir and M. Aydin, "A novel asymmetric and unconventional stator winding configuration and placement for a dual three-phase surface PM motor," *IEEE Trans. Magnetics*, vol. 53, no. 11, pp. 1–5, Nov. 2017.
[21] W. C. Lo, C. C. Chan, Z. Q. Zhu, Lie Xu, D. Howe, and K. T. Chau, "Acoustic noise radiated by PWM-controlled induction machine drives," *IEEE Trans. Ind. Electron.*, vol. 47, no. 4, pp. 880–889, Aug. 2000.
[22] W. Liang, P. C. K. Luk, and W. Fei, "Analytical investigation of sideband electromagnetic vibration in integral-slot PMSM drive with SVPWM technique," *IEEE Trans. Power Electron.*, vol. 32, no. 6, pp. 4785–4795, Jun. 2017.

**Xun Han** (S'17) was born in Hubei, China, in 1992. He received the B.E.E. degree in electrical and electronic engineering from Harbin Institute of Technology, Weihai, China, in 2015. He is currently working toward the Ph.D. degree with the School of Electrical and Electronic Engineering, Huazhong University of Science and Technology, Wuhan, China.

His current research interests include the control of novel permanent-magnet machines and power electronics.

**Dong Jiang** (S05'–M12'–SM16') received the B.S. and M.S. degrees in electrical engineering from Tsinghua University, Beijing, China, in 2005 and 2007, respectively, and the Ph.D. degree from the University of Tennessee, Knoxville, TN, USA, in December 2011.

He began his Ph.D. study in the Center for Power Electronics Systems (CPES) in Virginia Tech in 2007 and was transferred to the University of Tennessee with his Advisor in 2010. He was with United Technologies Research Center (UTRC) in Connecticut as a Senior Research Scientist/Engineer from January 2012 to July 2015. Since July 2015, he has been a Professor with Huazhong University of Science and Technology (HUST), Wuhan, China. His current research interests include power electronics and motor drives, with more than 60 published IEEE journal and conference papers in this area.

Dr. Jiang was the recipient of two Best Paper Awards in IEEE conferences. He is an Associate Editor of the IEEE TRANSACTIONS ON INDUSTRY APPLICATIONS.

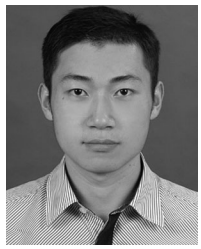

**Tianjie Zou** (S'15) was born in Hubei, China, in 1991. He received the B.E.E. degree in 2013 in electrical and electronic engineering from Huazhong University of Science and Technology, Wuhan, China, where he is currently working towards the Ph.D. degree in electrical engineering.

His current research interests include design, analysis, and intelligent control of permanent-magnet machines.

**Ronghai Qu** (S'01–M'02–SM'05–F'18) was born in China. He received the B.E.E. and M.S.E.E. degrees from Tsinghua University, Beijing, China, and the Ph.D. degree from the University of Wisconsin–Madison, Madison, WI, USA, in 1993, 1996, and 2002, respectively, all in electrical engineering.

In 1998, he joined the Wisconsin Electric Machines and Power Electronics Consortiums, University of Wisconsin–Madison, WI, USA, as a Research Assistant. He became a Senior Electrical Engineer at Northland, a Scott Fetzer Company, Watertown, NY, USA, in 2002. Since 2003, he had been with the General Electric (GE) Global Research Center, Niskayuna, NY, USA, as a Senior Electrical Engineer in the Electrical Machines and Drives Laboratory. Since 2010, he has been a Professor with Huazhong University of Science and Technology, Wuhan, China. He has authored or coauthored more than 230 published technical papers and is the holder of more than 50 patents/patent applications.

Dr. Qu is a Full Member of Sigma Xi. He was the recipient of several awards from the GE Global Research Center since 2003, including the Technical Achievement and Management Awards. He was also the recipient of the 2003 and 2005 Best Paper Awards, third prize, from the Electric Machines Committee of the IEEE Industry Applications Society (IAS) at the 2002 and 2004 IAS Annual Meeting, respectively.

**Kai Yang** received the B.Eng., M.Sc., and Ph.D. degrees in electrical and electronic engineering from Huazhong University of Science and Technology, Wuhan, China, in 1998, 2000, and 2003, respectively.

He is currently a Professor with the College of Electrical and Electronic Engineering, Huazhong University of Science and Technology and the Director of the Department of Electrical Machinery and Control. His current research interests include new type motors and their servo control systems.